PHYSICS

Attosecond interferometry of shape resonances in the recoil frame of CF_4

Saijoscha Heck[1], Denitsa Baykusheva[2]*, Meng Han[1], Jia-Bao Ji[1], Conaill Perry[1], Xiaochun Gong[1,3], Hans Jakob Wörner[1]*

Shape resonances play a central role in many areas of science, but the real-time measurement of the associated many-body dynamics remains challenging. Here, we present measurements of recoil frame angle-resolved photoionization delays in the vicinity of shape resonances of CF_4. This technique provides insights into the spatiotemporal photoionization dynamics of molecular shape resonances. We find delays of up to ~600 as in the ionization out of the highest occupied molecular orbital (HOMO) with a strong dependence on the emission direction and a pronounced asymmetry along the dissociation axis. Comparison with quantum-scattering calculations traces the asymmetries to the interference of a small subset of partial waves at low kinetic energies and, additionally, to the interference of two overlapping shape resonances in the HOMO-1 channel. Our experimental and theoretical results establish a broadly applicable approach to space- and time-resolved photoionization dynamics in the molecular frame.

INTRODUCTION

Shape resonances are quasi-bound states of matter created by the presence of a potential energy barrier. They play a crucial role in nuclear reactions (*1*), cold and ultracold chemistry (*2*, *3*), the existence of exotic ultralong-range molecules (*4*, *5*), and scattering of low-energy electrons with molecules (*6*, *7*). They are also relevant for understanding dissociative electron attachment, which dominates radiation damage of DNA in aqueous solution (*8*–*10*). In all of these cases, the presence of a potential barrier allows for an extended interaction time between the two unbound particles, which considerably affects the outcome of the reaction. Most of these interaction times are ultrashort, ranging from femtoseconds in electron attachment to well below 1 as in nuclear reactions (*11*). Hence, a real-time study of the associated many-body dynamics lies at the frontier of present-day capabilities.

A particularly interesting class of shape resonances arises in the context of molecular photoionization (PI). They are created by the combination of the short-range, Coulomb, and centrifugal potentials (*12*) and are therefore sensitive to subtle electron-correlation effects. Following photoabsorption, the electron can be trapped in a shape resonance until it tunnels through the associated potential barrier. The lifetime and the energy at which the resonance occurs are a fingerprint of the underlying multielectron dynamics.

Shape resonances have so far mainly been identified as local maxima in PI cross sections and/or rapid variations in the asymmetry parameter (*12*), but their definitive identification and characterization have remained challenging (*13*, *14*). With the advent of attosecond science, time-domain access to shape resonances has become possible (*15*–*18*), but a state- and angle-resolved characterization of these time delays has so far not been achieved.

In this work, we demonstrate an experimental method that completely resolves the attosecond PI dynamics of nonlinear molecules in their recoil frame and the final states of the cation. Our technique thereby simultaneously reveals the temporal and the angular manifestations of shape resonances in CF_4 and provides unprecedented information on their PI dynamics. Our experimental approach is based on attosecond interferometry, also known as RABBIT (reconstruction of attosecond beating by interference of two-photon transitions) (*19*–*21*), in combination with an electron-ion coincident three-dimensional (3D) momentum imaging detection scheme (COLTRIMS) (*22*, *23*), as recently applied to atoms and linear molecules (*24*–*28*). This combination of techniques makes it possible to access ionization time delays in the molecular frame of a molecule. Previous work on CO (*28*) has been limited to a left-right asymmetry, previously called "stereo" time delay (*29*). Accessing PI dynamics in the molecular frame can give detailed insight into the ionization process of molecules and has drawn recent theoretical interest (*16*, *29*–*31*). In contrast to prior work, we achieved full angular- and final-state resolution.

In RABBIT measurements, the amplitude of a given sideband (SB) oscillates as a function of the time delay τ between infrared (IR) and extreme ultraviolet (XUV) pulses as

$$I_{SB} = A + B \times \cos(2\omega_{IR}\tau - \Phi_{XUV} - \Phi_{Mol}) \quad (1)$$

where A and B are constants, ω_{IR} is the IR probe frequency, Φ_{XUV} is the spectral phase of the attosecond pulse train (APT; containing the attochirp), and Φ_{Mol} is the molecule-specific phase term. In our experiments, described in more detail in Materials and Methods, the XUV and IR fields are focused into a molecular beam, as shown in Fig. 1B. Using argon and CF_4 in a gas mixture allows us to reference the extracted PI time delays of CF_4 against the time delays in argon, which eliminates the contribution of the attochirp and minimizes the influence of the continuum-continuum delays due to the similar ionization potentials.

Upon ionization, CF_4 dissociates into CF_3^+ and F, which lowers the initial T_d symmetry to C_{3v}. The time scale of this dissociation has been recently determined to be only 40 fs (*32*), which is considerably faster than the rotational period of the molecule (*33*, *34*). As a consequence, the momentum vector of CF_3^+ is, in excellent approximation,

[1]Laboratorium für Physikalische Chemie, ETH Zürich, 8093 Zürich, Switzerland. [2]Department of Physics, Harvard University, Cambridge, MA 02138, USA. [3]State Key Laboratory of Precision Spectroscopy, East China Normal University, Shanghai, China. *Corresponding author. Email: dbaykusheva@g.harvard.edu (D.B.); hwoerner@ethz.ch (H.J.W.)

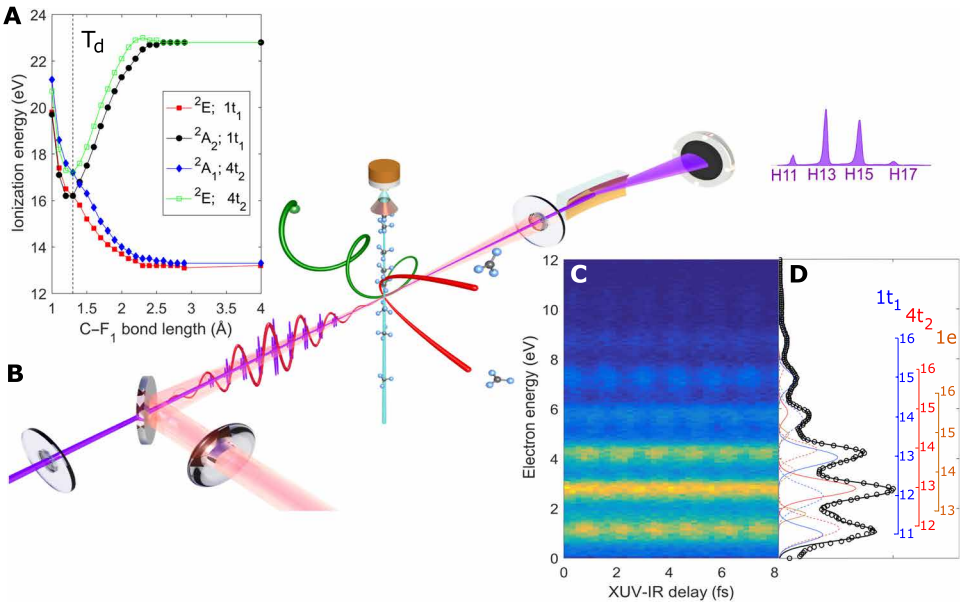

Fig. 1. Experimental overview. (**A**) Potential energy curves of the relevant states of CF_4^+ as a function of the C-F bond length. The state labeling is according to C_{3v} symmetry of the final state and T_d symmetry of the ionized orbital. The energy scale was chosen to reflect the experimental vertical ionization energies. Details of the calculations are given in section S1.5. (**B**) Sketch of the experimental setup. The ionic fragments and emitted photoelectrons are measured in coincidence as a function of the XUV-IR delay. The XUV APT is spectrally characterized via an online soft x-ray spectrometer. (**C**) RABBIT spectrogram of CF_4 for θ = 0 ° to 18°. (**D**) Photoelectron spectrum of CF_4 created by the APT. The photoelectron bands of the three energetically accessible states are fitted according to their partial cross sections and relative XUV intensities using sums of Gaussians.

oriented parallel to the C-F axis in the molecular frame (axial recoil approximation). This leads to a highly accurate determination of the electron emission direction with respect to the dissociating C-F axis in the recoil frame. By detecting the full 3D momentum vector of the ion in coincidence with the 3D momentum vector of the electron, we are therefore able to analyze attosecond photoelectron spectra (RABBIT traces) and extract PI time delays for specific electron emission angles θ in the recoil frame.

One of the main challenges in extracting PI time delays from molecular spectra is the spectral congestion that is caused by the broad bandwidth of XUV-APTs in combination with broad photoelectron spectra. We solved this problem by using the complex-valued principal components analysis (CVPCA) (*35*). A description of this analysis method is given in Materials and Methods. The experimental results are supported by ab initio quantum-scattering calculations of the RABBIT time delays that are angle-dependent, both in the laboratory frame and in the molecular frame (see methods and section S1 for more details).

RESULTS AND DISCUSSION

In a first step, we investigate the shape resonance found in the vicinity of the electronic ground state of CF_4^+, where we find a PI time delay of up to ~600 as, relative to argon, which is caused by the resonance. Next, we investigate the time delay in the recoil frame of CF_4, where we find a pronounced asymmetry in the delays for low kinetic energies. The ionization potentials of the four outer-valence orbitals of CF_4 ($...3t_2^6\ 1e^4\ 4t_2^6\ 1t_1^6$) are 22.12, 18.50, 17.49, and 16.20 eV, respectively (*36*, *37*). PI from one of these orbitals results in CF_4^+ in the states $\widetilde{C}^2T_2$, $\widetilde{B}^2E$, $\widetilde{A}^2T_2$, or $\widetilde{X}^2T_1$. None of these CF_4^+ states are stable. The $\widetilde{C}$ state dissociates into $CF_2^+ + F_2$ and $CF_2^+ + F + F$, while the $\widetilde{B}$, $\widetilde{A}$, and $\widetilde{X}$ states dissociate into $CF_3^+ + F$ (*38*, *39*). Because of the prominence of the latter two states in the photoelectron spectrum, we focus exclusively on the $\widetilde{A}$ and $\widetilde{X}$ states, the potential energy surfaces of which are shown in Fig. 1A. We did not observe any CF_2^+ in our ion mass spectra.

The PI cross section of the $1t_1$ orbital has a prominent maximum in the $1t_1 \rightarrow kt_2$ (where k indicates a continuum state) channel around 2.5 eV (see the blue curve in Fig. 2A), which corresponds to the energy of an electron from SB12. This overlap in the energy makes this particular SB perfectly suited to investigate the signatures of the shape resonance. At this point, we note that the exact energy of the resonance is debated in the literature (*34*, *40*), but our theoretical results and experimental observation (see Fig. 1D) are consistent with those reported by Carlson *et al.* (*40*) and Larsen *et al.* (*34*) that suggest that the PI cross section is enhanced below 3 eV owing to the influence of the shape resonance. The results are shown in Fig. 2A, where the ionization delays of the CF_4 $1t_1$ channel referenced to the delay of the 3p electron in argon are shown as a function of the electron kinetic energy. Argon was chosen because of its similar ionization potential [15.76 eV; (*41*)] to the $\widetilde{X}$ state of CF_4^+, which leads to a near cancellation of the continuum-continuum contribution τ_{cc} to the measured delays, because τ_{cc} only depends on the electron kinetic energy (*16*, *42*). In our calculations, we account for the small difference in ionization potentials by referencing CF_4 electrons with energy $E_{kin}^{CF_4}$ to argon electrons with energy $E_{kin}^{Ar} = E_{kin}^{CF_4} + I_p^{CF_4} - I_p^{Ar}$ (where $I_p^{CF_4}$ refers to either HOMO and HOMO-1). All delays shown throughout this manuscript, both experimental and theoretical, are referenced to the argon delays with electron emission parallel to the XUV polarization direction.

For channel $1t_1$, a delay of 614 (±190) as is observed at the energy of the shape resonance, which is substantially larger than any previously

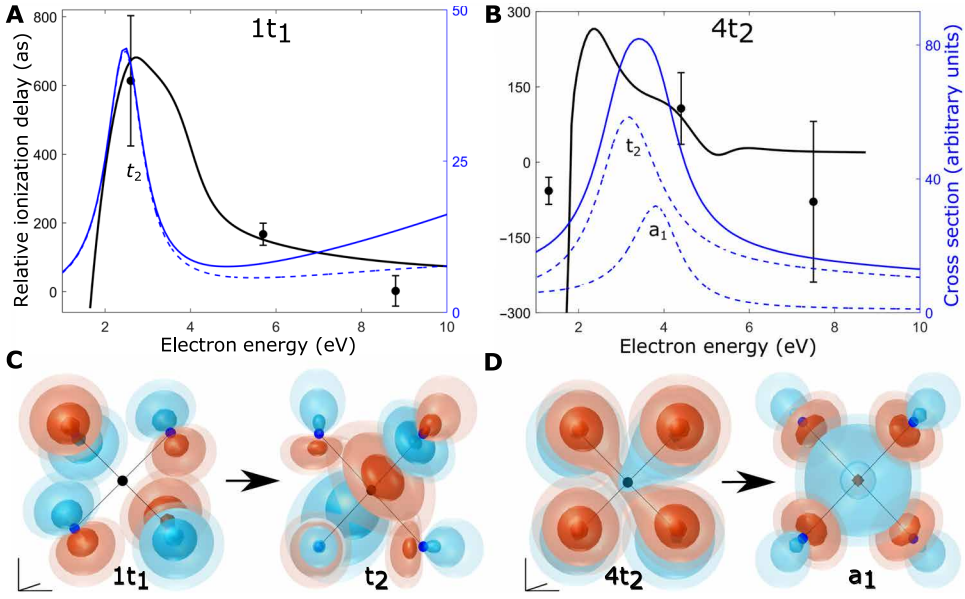

Fig. 2. Laboratory frame ionization delays and shape resonances. PI delays of the (**A**) $1t_1$ channel and (**B**) $4t_2$ channel. Black filled circles show the experimental values, the black solid line shows the calculated RABBIT delays, including the cc (continuum-continuum) contribution (see Materials and Methods for detailed information), the blue solid line is the total cross section including all symmetries, and the blue dashed lines are the symmetry-resolved cross sections for t_2 and a_1. All cross sections are calculated within the same theoretical framework as the delays. Both experimental and theoretical delays are for electrons emitted 0° to 18° with respect to the XUV polarization and are referenced to argon using the same angular integration range. The error bars show the SD of the delays extracted from multiple datasets. (**C**) Three-dimensional orbital wave functions for the $1t_1$ HOMO (left) and the t_2 dipole-prepared wave function at the resonance energy (right). The electric field vector of the dipole transition was chosen to lie along one of the C-F bonds, thus creating a superposition of all three degenerate wave function components $1/\sqrt{3}(1\,t_1^{(x)} + 1\,t_1^{(y)} + 1\,t_1^{(z)})$. (**D**) Same as (C), but for $4t_2$ HOMO-1 and its dipole-prepared resonant a_1 wave function. Contour levels used are 0.8, 0.7, 0.35, 0.15, and 0.09. Alternative versions of (C) and (D) using different contour-level values are shown in fig. S16.

measured time delays, even in the presence of shape resonances (*15*, *17*, *18*).

In Fig. 2C, we show the wave functions of the bound orbitals, as well as those of the t_2 PI continuum at resonance (the calculation procedure is described in section S1.4). It is evident that the continuum wave function has a local maximum at the position of the carbon atom, which is a signature of the cage effect (*43*). It additionally has sizable amplitudes on each of the fluorine atoms, which is a necessary condition for being optically accessible from the $1t_1$ orbital that has no wave function amplitude on the carbon atom. This shape resonance is thus truly molecular in character and bears little resemblance to the typical atomic shape resonances arising solely from potential barriers induced by the centrifugal term. The continuum part of the wave function is not visible in the plots because of its lower amplitude. A different version of the plots, with a lower iso-contour threshold and hence more visible continuum parts of the wave function, is shown in fig. S16. The measured and calculated RABBIT delays agree well with the calculated lifetime of the shape resonance (650 as; see table S1). This agreement is, however, fortuitous because the choice of a larger angular integration range leads to smaller RABBIT delays (210 as for complete angular averaging). In general, it is difficult to find a simple relationship between RABBIT delays and resonance lifetimes. A possible reason for this is the interference between resonant and nonresonant PI channels (in the sense of a Fano treatment) (*44*). In cases where the nonresonant contributions are not negligible (as is the case in CF_4; see figs. S8 and S9), the Wigner delays deviate from the resonance lifetimes. This is the case because the phase of the PI matrix elements is affected by the interference between resonant and nonresonant contributions, which leads to time delays that can noticeably deviate from the lifetime of the shape resonance.

The $4t_2$ channel has two overlapping shape resonances with symmetries t_2 and a_1 and partial cross sections shown in Fig. 2B. Experimentally, we measured a delay of 107 (±71) as close to resonance and negative delays of −57 (±27) as for energies below and −79 (±160) as above the resonances. In Fig. 2D, we show the $4t_2$ orbital and the a_1 continuum wave function at the energy of the corresponding shape resonance. The transition to the t_2 shape resonance is shown in fig. S15. Both shape resonances in the $4t_2$ channel also have a local maximum at the position of the carbon atom, as well as amplitude on the fluorine atoms. They also display a strong molecular character and the characteristic signatures of the cage effect.

Our RABBIT calculations agree very well with the experiment for both HOMO and HOMO-1 with the exception of the very low kinetic energy (1.3 eV) of SB12 of the HOMO-1. This energy cannot be accessed by our RABBIT calculation, because the IR-absorption pathway would involve intermediate states located below the HOMO-1 ionization threshold. Experimentally, this is possible by populating high-lying autoionizing Rydberg resonances below the $4t_2$ threshold, a process that is challenging to describe theoretically. A decrease toward negative delays for very low electron energies is nevertheless correctly described, and overall, we find excellent agreement between theory and experiment, which is remarkable for this low-energy range.

Next, we look into the recoil frame angle-resolved PI delays (RAPIDs), where we extract the PI time delays for specific electron

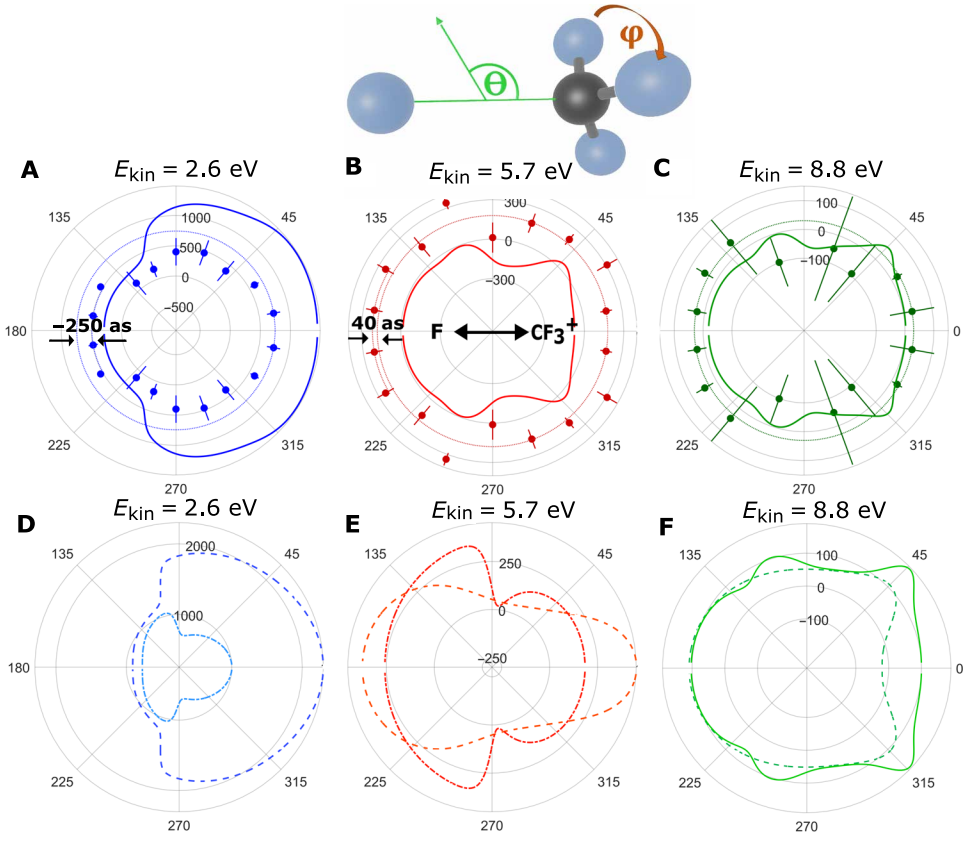

Fig. 3. RAPIDs of $1t_1$. PI delays of the $1t_1$ (HOMO) channel (relative to argon) shown in the recoil frame of CF_4. Experimental data (filled circles) are shown together with the calculated RABBIT delays, including all symmetries, partial waves, and continuum-continuum contribution (thick line), in (**A**) for SB12, (**B**) SB14, and (**C**) SB16. Kinetic energies pertain to CF_4 electrons. A dashed circle is drawn into the plots to guide the eye. (**D** to **F**) Theoretical RABBIT delays relative to argon for the partial-wave combinations of $l = 2$ and 3 (dot-dashed line), $l = 1$ to 3 (dashed line), $l = 1$ to 4 [thin line; only in (F)] for the t_2 continuum symmetry. For the partial-wave resolved delays, shown in (D) and (E), the continuum-continuum contribution and the argon reference delays are omitted. The schematic drawing of a CF_4 molecule visualizes the relevant angles. θ is plotted in the polar plots, and ϕ is averaged over, both in experiment and in theory. In all cases, the molecular dissociation axis is chosen parallel to the XUV polarization. All plots are mirrored vertically, and error bars show the SD of the delays extracted from multiple datasets. More information on the error analysis and the theoretical calculations is presented in Materials and Methods.

emission directions relative to the dissociation axis of CF_4^+ being parallel to the XUV polarization, as illustrated in Fig. 3. Because CF_3^+ remains intact, we cannot access the absolute orientation of CF_3^+ about that axis. In our calculations, this is accounted for by isotropically averaging over the azimuthal angle ϕ. This approach has previously been successfully applied to the dissociative ionization of CF_4 (*34*, *45*) and resulted in very precise RFPADs (recoil frame photoelectron angular distributions).

Figure 3 shows the RAPIDs for SB12, SB14, and SB16 of the $1t_1$ channel. The most notable feature is the asymmetry of the ionization delays along the dissociation axis with the delay being 250 as larger for the electron emitted along the CF_3^+direction in SB12 (Fig. 3A). This asymmetry changes direction for higher electron energies, i.e., at SB14, where the delay is ~40 as larger for electrons emitted in the direction of the neutral fluorine fragment (Fig. 3B). For the even higher electron energies of SB16, the asymmetry becomes even smaller in the experiment, and the delays for emission along the molecular dissociation axis are almost symmetric (Fig. 3C).

These results are qualitatively reproduced in our calculations and can be explained by a partial wave decomposition of the RABBIT delays. The asymmetry is caused by the interfering contributions of several partial waves at the resonance. At the resonant energy, the contributions of partial waves with $l = 2$ and $l = 3$ are enhanced (fig. S8), which causes the RAPID to be dominated by only those two partial waves (Fig. 3D). The interference of two partial waves of opposite parity is known to cause maximal asymmetries in the photoelectron angular distributions (*46*), which is also true in molecular frame photoelectron angular distributions (MFPADs). Our calculations show that such asymmetries also appear in the RAPIDs. The lack of quantitative agreement highlights the difficulty of electron molecule scattering calculations at very low kinetic energies, particularly in the presence of resonances.

It is indeed mainly the sum of those two partial waves, which causes the strong asymmetry observed, as can be seen in Fig. 3D. In this case, the PI dipole matrix element experiences a sign change as a function of energy, which is responsible for a phase shift and results in an inversion of the delay asymmetry from SB12 (Fig. 3, A and D) to SB14 (Fig. 3, B and E).

Adding more partial waves suppresses the delay asymmetry, yielding almost isotropic delays at the highest SB resolved in the experiment (SB16) shown in Fig. 3C. The shape of the RABBIT

delays in Fig. 3 (E and F) is qualitatively very similar, which is a consequence of partial waves contributing with equal weights at energies above the resonance. The energy-dependent asymmetry observed in the RAPIDs must therefore be a final-state effect, as opposed to the interpretation of the stereo time delays in CO (*28*), which was based on a pure initial-state effect.

A similar behavior is observed in the RAPIDs of the $4t_2$ channel, shown in Fig. 4, where the ionization delay asymmetry between the CF_3^+ and F direction is 105 as in SB12 and 160 as in SB14 (larger delays toward the CF_3^+ fragment) before it becomes symmetric in SB16. The $4t_2$ channel is particularly interesting to study because it contains two overlapping shape resonances of different continuum symmetries, i.e., a_1 and t_2. The two resonances are close in energy, couple to the same total final-state symmetry, and show strong intrachannel coupling as identified in RFPAD measurements (*34*). The two resonances have different partial-wave contributions as shown in fig. S9, with the main contributions for symmetry a_1 being $l = 0$, 3, and 4, while for symmetry t_2, it is $l = 1$, 2, and 3. Qualitatively, the asymmetry in the RAPID of SB12 can be described by a single-channel calculation for a_1 symmetry using only the dominant partial waves $l = 0$, 3, and 4 (see fig. S9). This is not the case for SB14 with an electron energy of $E_{kin} = 4.4$ eV just on the resonance. Neither single-channel calculations for a_1 or t_2 are able to qualitatively reproduce the experimental RAPID. Even the full RABBIT calculation, including all partial waves and symmetries (Fig. 4B), does not result in perfect agreement, because the peaks at $\theta = 60^\circ$ and $\theta = 120^\circ$ are reproduced, but the local maximum at $\theta = 0^\circ$ is not.

This result highlights the pronounced sensitivity of RAPIDs to the finest details of the PI dynamics. Whereas the agreement of the calculated laboratory frame delay at SB14 with experiment is excellent (Fig. 2B), the deviation in the angle-resolved delays amounts to more than 600 as. A discrepancy between experiment and theory close to $\theta = 0^\circ$ is also visible in the RFPADs recorded in the immediate vicinity of SB14 ($E_{kin} = 4.3$ eV; see fig. S6C). Notably, our calculations agree almost perfectly with the RFPAD calculations including channel coupling (*34*), but neither of the calculations reproduces the local maximum of the RFPAD in the vicinity of $\theta = 0^\circ$. In an attempt to go beyond the fixed nuclei approximation, we also varied the C-F bond lengths within the Franck-Condon region, which, however, did not result in better agreement. Because both RFPADs and RAPIDs are sensitive to the amplitudes and phases of the PI matrix elements, the observed discrepancies suggest that the accuracy of molecular PI calculations needs to be improved further and that RAPIDs are a particularly sensitive benchmark for such work.

For higher energies of SB16 ($E_{kin} = 7.5$ eV), the agreement between RABBIT delays and experiment is again quite good. The delays are almost symmetric with respect to emission along the dissociation axis, which is a result of the contribution of multiple partial waves, similar to the case of the HOMO channel. A notable feature unique to the RAPIDs of HOMO-1 is the pronounced local maxima at $\theta = 60^\circ$ and $\theta = 120^\circ$, particularly obvious in the complete calculation shown in Fig. 4B.

Those "ears" are a direct result of the interference between the two shape resonances of different symmetries and only appear

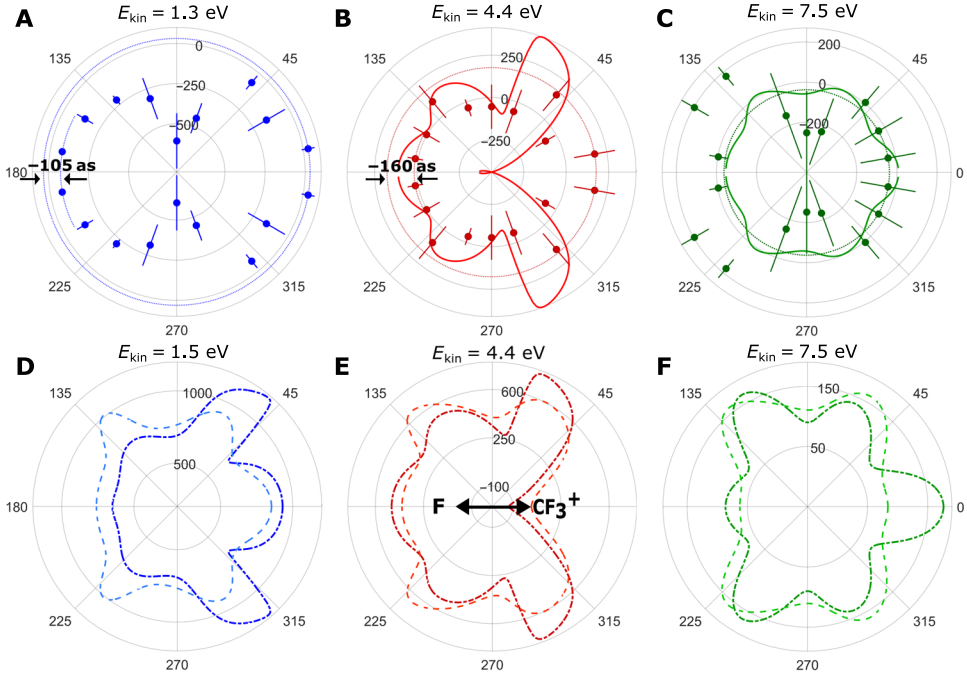

Fig. 4. RAPIDs of $4t_2$. PI delays of the $4t_2$ channel referenced to argon shown in (**A**) for SB12, (**B**) SB14, and (**C**) SB16. Kinetic energies given are for CF_4 electrons. A dashed circle is drawn into the plots to guide the eye. The filled circles represent the experimental data, and the solid line represents the calculated RABBIT delays, including all symmetries, partial waves, and the continuum-continuum contribution. (**D** to **F**) Coherent (dot-dashed line) and incoherent (dashed line) sum of RABBIT delays of continuum symmetries a_1 and t_2 restricted to the contributions of partial waves $l = 0$ to 4. For the partial-wave resolved delays, shown in (D) and (E), the continuum-continuum contribution and the argon reference delays are omitted. In both experiment and theory, the molecular dissociation axis is parallel to the XUV polarization. All plots are mirrored vertically. Note that the RABBIT calculation is not defined for (A) due to the low energy. For this reason, an energy of 1.55 eV was chosen for (D).

clearly when adding both symmetries coherently. This is shown in Fig. 4 (D and E) through a comparison of the incoherent and coherent sums of symmetries a_1 and t_2.

In conclusion, we have reported the first angle- and state-resolved measurements of molecular PI delays. We have applied this new capability to characterize the PI dynamics of CF_4 in the vicinity of several shape resonances. In the case of the HOMO channel, we measured time delays of up to 614 as caused by electron trapping enhanced by a molecular cage effect. In the case of the HOMO-1 channel, we have additionally identified the effects of the interference between two shape resonances of different continuum symmetries on the molecular-frame–resolved PI delays.

The highly structured and asymmetric time delays in the recoil frame of the molecule and in the vicinity of the shape resonances are qualitatively reproduced by our first-principles quantum-scattering calculations. They are explained in terms of a partial-wave analysis, tracing the reason for the asymmetry to the dominant contribution of only two to three partial waves at the resonances. The good overall agreement of experiment and theory, combined with the notable disagreement close to the overlapping shape resonances in the HOMO-1 channel, demonstrates the sensitivity of RAPIDs to the finest details of molecular PI dynamics and therefore their considerable potential as benchmarks for future theory developments. These results establish RAPIDs as a sensitive observable for characterizing multielectron attosecond dynamics in molecules and improving the description of electron correlation in theoretical methods. The demonstrated experimental and theoretical methods can be readily extended to more complex molecular systems, including, e.g., nucleoside anions, which could be used to time resolve the attosecond dynamics underlying dissociative electron attachment and the resulting DNA strand breaks that mediate radiation damage.

MATERIALS AND METHODS

Attosecond pulse generation

The optical setup consists of a regeneratively amplified Titanium-Sapphire laser system, which delivers 1.2-mJ pulses at 5-kHz repetition rate with a pulse duration of 35 fs (full width at half maximum) and a central wavelength of 800 nm. The laser beam is divided into two pathways with a 70:30 beam splitter, where the more intense part is focused into xenon gas for high harmonic generation (HHG), resulting in odd harmonics up to 17th order (≡26.3 eV). After the HHG cell, a 100-nm-thick metallic filter (either aluminum or tin) is placed in front of a nickel-coated toroidal mirror (f = 50 cm) to eliminate any residual IR in the XUV path. The less intense part of the initial beam is recombined with the XUV pulse after the toroidal mirror to constitute a Mach-Zehnder interferometer. The path length difference is controlled by a piezoelectric motor (resolution 0.1 nm). The relative delay between the IR and XUV pulses is actively stabilized in an interferometric approach using a frequency-stabilized helium-neon laser coupled into the XUV-IR Mach-Zehnder interferometer (*47*), resulting in a time jitter ranging from 40 to 60 as.

Coincidence spectrometer

The phase-locked XUV and IR pulses are colinearly focused into a supersonic gas jet in a COLTRIMS (cold target recoil ion momentum spectroscopy) spectrometer (*22*, *23*), where the electrons and ions are guided by a weak homogeneous electric field (1 to 3 V/cm) onto two opposite position and time-of-flight sensitive detectors. A homogeneous magnetic field (4.2 to 5.9 G) is additionally applied via a pair of Helmholtz coils, which is tilted to compensate for Earth's magnetic field. Each detector consists of two 75-mm-diameter microchannel plates (Photonis) in Chevron configuration in combination with a three-layer delay-line anode (Hexanode) with a crossing angle of 60° between the adjacent layers and an active radius of 40 mm (RoentDek). The spectrometer for the electron side consists of a 70-mm extraction region, followed by a 140-mm electric field–free region. On the ion side, the length of the extraction region is 40 mm. Using COLTRIMS, we gain access to the full 3D momentum vectors of ions and electrons in 4π solid angle. To ensure coincidence detection of ions and electrons, the maximum ion count rate was set to 0.3 counts per laser shot. The Ar-CF_4 gas mixture is supersonically expanded into the vacuum chamber through a 50-μm-diameter nozzle with a backing pressure of 1 bar. Two conical skimmers are located 10 and 30 mm behind the nozzle with orifices of 500 μm and 1 mm, respectively, as a part of a differential pumping scheme. The supersonic gas jet is captured by a differentially pumped beam dump after crossing the spectrometer.

Data analysis

Ten datasets of CF_4-Ar gas mixtures were measured, partially under different experimental conditions, to optimize the data quality at the low- and high-energy ranges. Parameters that were varied are the HHG phase-matching conditions, such as the xenon gas pressure and the IR intensity, the metallic filter (either Al or Sn), the electric extraction field in the COLTRIMS, and the magnetic field. The data were then analyzed for argon and CF_4 separately using a CVPCA, which has been introduced by Jordan and Wörner (*35*) and since then successfully used to extract phases in spectrally congested time-resolved electron spectra (*48*–*50*). The CVPCA is implemented as follows. First, we fit the static XUV-only photoelectron spectra using a set of Gaussians to get the correct fit parameters describing the relative XUV spectral intensities, cross sections, and spectral widths of the states involved. Second, we fit the 1D energy spectrum of the time-resolved XUV-IR measurement, obtained by integration over all time delays, using the fitting parameters from the XUV-only fits plus an additional set of Gaussians accounting for the SBs (see fig. S17B). Then, a fast Fourier transform (FFT) is done line by line on the photoelectron spectra along the time delay axis. The obtained band in the complex-valued FFT at the 2ω angular frequency is fitted by multiplying each Gaussian component obtained in the XUV + IR fit with a complex-valued amplitude e^{zj}

$$I_{\mathrm{fit}}(E) = \sum_j p_j(E)\, e^{z_j} = \sum_j \underbrace{e^{a_j} p_j(E)}_{A_j(E)}\, e^{ib_j} \tag{2}$$

where $p_j(E)$ is the Gaussian fit for the photoelectron band j (see fig. S17, C and D). This procedure is done for each of the 10 datasets individually resulting in 10 phase values at SB14 and 5 phase values at SB12 and SB16 phases for argon and each electronic state of CF_4^+. The lower number of phase values for SB12 and SB16 is a result of specifically optimizing five measurements for high and low electron energy conditions, respectively.

The extracted phases of argon are then subtracted from the corresponding CF_4 phases to eliminate the intrinsic attochirp and converted into time delays using a conversion factor of 215 as. The conversion factor is derived using $T/2\pi$, where T is half the period

of the probing IR field. Its value was determined through a cosine fit of the SB beating in argon to be $T = 1350.9$ as. Argon was chosen as a reference because of its simple photoelectron spectrum and similar ionization potential to the $1t_1$ (HOMO) of CF_4. For the final delay values, we take the average of all measurements, and the error is calculated as

$$\sigma_{\bar{\tau}} = \frac{\sigma}{\sqrt{n}} \tag{3}$$

where σ is the SD and n is the total number of datasets used to calculate the mean. The particularly large error bars of SB12 in the HOMO and SB16 in HOMO-1 are a result of the strong overlap of those SBs with a more intense main band of the other state, as can be seen in fig. S17B.

Recoil frame angle-resolved PI delays

To resolve PI time delays in the recoil frame of CF_4, we extract phases only for specific electron emission directions with respect to the recoil axis. In all RAPIDs, nine values for the angle between electron and CF_3^+ emission directions were chosen, each with a width of 20°, to get a continuous coverage of the angular space. In addition, the recoil frame was fixed to the XUV polarization to allow for less ambiguity and more direct comparison to theory, where the molecular axis was fixed parallel to the XUV polarization. The accepted angle between CF_3^+ and XUV polarization is 0° to 25° and 155° to 180°. All angle-resolved CF_4 delays in the RAPID are referenced to the same argon delay using

$$\tau_{\mathrm{ref}}^{\mathrm{SBx}}(\theta) = \tau_{\mathrm{CF_4}}^{\mathrm{SBx}}(\theta) - \tau_{\mathrm{Ar}}^{\mathrm{SBx}}(\beta = 0°\text{–}18°) \tag{4}$$

where θ is the angle between electron emission and the molecular dissociation axis and β is the angle between electron emission and XUV polarization. SBx is the respective SB. All delays shown in the manuscript are the referenced values $\tau_{\mathrm{ref}}^{\mathrm{SBx}}$.

Calculation of the RABBIT delays

The emission angle–resolved SB intensity $I_{\mathrm{SB},n}^{\hat{R}}(E_{\mathrm{SB}}, \vartheta, \varphi; \tau)$ for a single molecular orientation [denoted in what follows by the Euler angle set $\hat{R} \equiv (\alpha, \beta)$] is given by the coherent sum of the two interfering pathways

$$I_{\mathrm{SB},n}^{\hat{R}}(E_{\mathrm{SB}}, \vartheta, \varphi; \tau) = \sum_{\Gamma_0} \left| \widehat{M}_{\mathrm{a}}^{\Gamma_0}(E_<, \vartheta, \varphi)\, e^{+i\omega_0\tau} + \widehat{M}_{\mathrm{e}}^{\Gamma_0}(E_>, \vartheta, \varphi)\, e^{-i\omega_0\tau} \right|^2 \tag{5}$$

where ϑ, φ denote the set of electron emission angles with respect to the molecular frame (defined in Fig. 3), and $\widehat{M}_{\mathrm{a}}^{\Gamma_0}$ and $\widehat{M}_{\mathrm{e}}^{\Gamma_0}$ are the amplitudes of the absorption and emission angles, respectively, whereby the "^" signifies that these quantities are evaluated for a single molecular orientation $\hat{R}$. τ is the temporal delay between XUV and IR fields, and ω_0 is the center frequency of the IR pulse driving the HHG process (here, its value is set to correspond to ≈1.55 eV or 800 nm). Furthermore, $E_{\mathrm{SB}} = n\omega_0 - I_p$ denotes the energy corresponding to the n^{th} SB, and $E_{\lessgtr} = E_{\mathrm{SB}} \mp \omega_0$. The summation over the irreducible representations Γ_0 in Eq. 5 reflects the fact that the initially occupied HOMO and HOMO-1 of CF_4 are threefold degenerate (with symmetries t_1 and t_2, respectively).

Experimentally, the collected signal representing the MF-resolved SB intensity contains contributions from all orientations of the CF_3^+ fragment around the recoil axis. To account for this situation, the calculated SB intensity is isotropically averaged over the azimuthal angle φ

$$I_{\mathrm{SB},n}^{\hat{R}}(E_{\mathrm{SB}}, \vartheta; \tau) = \sum_{\Gamma_0} \int_0^{2\pi} \left| \widehat{M}_a^{\Gamma_0}(E_<, \vartheta, \varphi)\, e^{+i\omega_0\tau} + \widehat{M}_e^{\Gamma_0}(E_>, \vartheta, \varphi)\, e^{-i\omega_0\tau} \right|^2 d\varphi \tag{6}$$

In a manner analogous to the experimental data analysis procedure, the angle-resolved SB delay time is extracted from the calculated SB (see Eq. 6) by means of a fit using a harmonic function of the form

$$I_{\mathrm{SB},n}^{\hat{R}}(E_{\mathrm{SB}}, \vartheta; \tau) = a_0 + a_1 \cos(2\,\omega_0\,\tau - \Delta\Phi_{\mathrm{Mol}}(E_{\mathrm{SB}}, \vartheta)) \tag{7}$$

The corresponding angle-resolved delay associated with SB n is then given by $\tau_{\mathrm{SB}}^n(\vartheta) = \frac{\Delta\Phi_{\mathrm{Mol}}(E_{\mathrm{SB}}, \vartheta)}{2\,\omega_0}$. It is this quantity that we refer to as "RABBIT" delay throughout the manuscript. As the expression in Eqs. 5 and 6 features an incoherent sum over the contributing degenerate orbitals (Γ_0), it is generally not possible to give a convenient closed-form analytical expression for τ_{SB}. The emission angle–dependent calculated intensities for SB12, SB14, and SB16 for the RABBIT process involving PI from the HOMO and HOMO-1 orbital of CF_4 are reproduced in figs. S1 and S2. The black curves indicate the position of the maximizing phase $\Phi_{\mathrm{Mol}}(E_{\mathrm{SB}}, \vartheta)$ at each angle.

The theoretical molecular frame–resolved RABBIT delays presented in the main text have been evaluated for a configuration where the laser electric field vector (defining the laboratory frame) points along the dissociating C-F bond, i.e., for coincident laboratory and molecular frames ($\alpha = 0$, $\beta = 0$). The partially averaged delays introduced in Fig. 2 have been averaged over all orientations (Euler angles α, β) using a 50-point Lebedev grid, whereby the integration over the laboratory frame emission angles has been restricted to an emission cone with an opening angle of 18°, as in the experiment.

In principle, the above approach closely follows the formalism introduced in (*16*). There are, however, two distinctions. First, Eq. 6 takes into account the degeneracy of the initially occupied orbital, which plays an important role in nonlinear molecules. Second, in the current manuscript, we adopt the following approximation for the "two-photon" (XUV + IR) matrix elements: $\widehat{M}_{a/e}^{\Gamma_0}(E_{\mathrm{SB}}^{\lessgtr}, \vartheta, \varphi) \approx M_{1h\nu,a/e}^{\Gamma_0}(E_{\mathrm{SB}}^{\lessgtr}, \vartheta, \varphi)\, T_{\mathrm{cc}}(E_{\mathrm{SB}}, E_{\mathrm{SB}}^{\lessgtr})$, where $M_{1h\nu,\,a/e}$ is the one-photon PI matrix element and $T_{\mathrm{cc}}(E_{\mathrm{SB}}, E_{\mathrm{SB}}^{\lessgtr})$ is the long-range "continuum-continuum" contribution introduced in (*51*). In other words, we ignore the angular momentum couplings in the second step of the XUV + IR-PI process. The continuum-continuum matrix element is evaluated using the "P+A′" formula (see equation 100 and following text) in (*51*). The calculation of the one-photon PI matrix elements (in what follows, these will be referred to as "PI matrix elements" for brevity) follows the procedure outlined in section S1.1 and is identical with the formalism of (*16*).

The reference RABBIT delays for Ar are calculated following a conceptually analogous procedure, whereby we directly use the formula for the two-photon matrix elements given in equation 24 of (*42*). For completeness, we reproduce this expression below. Note that we have omitted the energy-independent terms and other constant factors and have slightly adapted the notation to ensure consistency with the rest of this text

$$M_{a/e}^{m_i}(E_{\mathrm{SB}}^{\lessgtr},\vartheta,\varphi) = N_{k_{\mathrm{SB}}^{\lessgtr}} N_{k_{\mathrm{SB}}} \frac{1}{|k_{\mathrm{SB}} - k_{\mathrm{SB}}^{\lessgtr}|^2} \exp\left[-\frac{\pi Z}{2}\left(\frac{1}{k_{\mathrm{SB}}^{\lessgtr}} - \frac{1}{k_{\mathrm{SB}}}\right)\right] \frac{(2k_{\mathrm{SB}}^{\lessgtr})^{iZ/k_{\mathrm{SB}}^{\lessgtr}}}{(2k_{\mathrm{SB}})^{iZ/k_{\mathrm{SB}}}} \quad (8)$$

$$\frac{\Gamma[2 + iZ(1/k_{\mathrm{SB}}^{\lessgtr} - 1/k_{\mathrm{SB}})]}{(k_{\mathrm{SB}}^{\lessgtr} - k_{\mathrm{SB}})^{iZ(1/k_{\mathrm{SB}}^{\lessgtr} - 1/k_{\mathrm{SB}})}} \sum_{L=l_i,l_i\pm 2} Y_{Lm_i}(\vartheta,\varphi) \sum_{\lambda=l_i\pm 1} \langle Y_{Lm_i}|Y_{10}|Y_{\lambda m_i}\rangle \langle Y_{\lambda m_i}|Y_{10}|Y_{l_i m_i}\rangle$$

$$\langle R_{k_{\mathrm{SB}}^{\lessgtr}}|r|R_{n_i l_i}\rangle\, i^{-\lambda} e^{i\eta_\lambda(k_{\mathrm{SB}}^{\lessgtr})}$$

In the above equation, k_{SB} and $k_{\mathrm{SB}}^{\lessgtr}$ correspond to the momenta associated with the energies E_{SB} and $E_{\mathrm{SB}}^{\lessgtr}$, i.e., $k_{\mathrm{SB}} = \sqrt{2E_{\mathrm{SB}}}$ and $k_{\mathrm{SB}}^{\lessgtr} = \sqrt{2E_{\mathrm{SB}}^{\lessgtr}}$. $Y_{lm}(\vartheta,\varphi)$ represent spherical harmonics, $Z = 1$, and $\Gamma(x)$ is the complex Gamma function. $\eta_\lambda(k_{\mathrm{SB}}^{\lessgtr})$ denotes the scattering phase shift, and $\langle R_{k_{\mathrm{SB}}^{\lessgtr}}|r|R_{n_i l_i}\rangle$ corresponds to the radial matrix element for the dipole transition involving the bound-state wave function $R_{n_i l_i}$ (here, $n_i = 3$ and $l_i = 1$) and the continuum function $R_{k_{\mathrm{SB}}^{\lessgtr}}$ with asymptotic momentum $k_{\mathrm{SB}}^{\lessgtr}$. We extract the one-photon PI matrix elements $\langle Y_{\lambda m_i}|Y_{10}|Y_{l_i m_i}\rangle\langle R_{k_{\mathrm{SB}}^{\lessgtr}}|r|R_{n_i l_i}\rangle\, i^{-\lambda} e^{i\eta_\lambda(k_{\mathrm{SB}}^{\lessgtr})}$ from our ePolyScat calculations (see section S1.1) (*52*, *53*). The associated SB intensity is calculated from the incoherent sum of the contributions of all three degenerate p orbitals ($m_i = 0, \pm 1$). The corresponding reference delays are subsequently extracted from a fit procedure as in the case of CF_4.

SUPPLEMENTARY MATERIALS

Supplementary material for this article is available at https://science.org/doi/10.1126/sciadv.abj8121

REFERENCES AND NOTES

1. W. Scheid, *FUNDAMENTALS OF PHYSICS—VOL. III—Nuclear Reactions* (Eolss Publisher Co. Ltd., 2009).
2. A. B. Henson, S. Gersten, Y. Shagam, J. Narevicius, E. Narevicius, Observation of resonances in penning ionization reactions at sub-kelvin temperatures in merged beams. *Science* **338**, 234–238 (2012).
3. X.-C. Yao, R. Qi, X.-P. Liu, X.-Q. Wang, Y.-X. Wang, Y.-P. Wu, H.-Z. Chen, P. Zhang, H. Zhai, Y.-A. Chen, J.-W. Pan, Degenerate Bose gases near a d-wave shape resonance. *Nat. Phys.* **15**, 570–576 (2019).
4. E. L. Hamilton, C. H. Greene, H. R. Sadeghpour, Shape-resonance-induced long-range molecular Rydberg states. *J. Phys. B Atomic Mol. Phys.* **35**, L199–L206 (2002).
5. M. Peper, J. Deiglmayr, Heteronuclear long-range Rydberg molecules. *Phys. Rev. Lett.* **126**, 013001 (2021).
6. G. J. Schulz, Resonances in electron impact on atoms. *Rev. Mod. Phys.* **45**, 378–422 (1973).
7. R. E. Palmer, P. J. Rous, Resonances in electron scattering by molecules on surfaces. *Rev. Mod. Phys.* **64**, 383–440 (1992).
8. B. Boudaïffa, P. Cloutier, D. Hunting, M. A. Huels, L. Sanche, Resonant formation of DNA strand breaks by low-energy (3 to 20 eV) electrons. *Science* **287**, 1658–1660 (2000).
9. S. Tonzani, C. H. Greene, Low-energy electron scattering from DNA and RNA bases: Shape resonances and radiation damage. *J. Chem. Phys.* **124**, 054312 (2006).
10. F. Martin, P. D. Burrow, Z. Cai, P. Cloutier, D. Hunting, L. Sanche, DNA strand breaks induced by 0-4 eV electrons: The role of shape resonances. *Phys. Rev. Lett.* **93**, 068101 (2004).
11. P. Kleinwachter, I. Rotter, On resonance phenomena in nuclear reaction cross sections. *J. Phys. G* **8**, 955–966 (1982).
12. J. L. Dehmer, Shape resonances in molecular fields. *ACS Symp. Ser.* **263**, 139–163 (1984).
13. M. Braunstein, V. McKoy, Shape resonances in the photoionization of N_2O. *J. Chem. Phys.* **87**, 224–228 (1987).
14. M. Piancastelli, The neverending story of shape resonances. *J. Electron Spectrosc. Relat. Phenom.* **100**, 167–190 (1999).
15. M. Huppert, I. Jordan, D. Baykusheva, A. Von Conta, H. J. Wörner, Attosecond delays in molecular photoionization. *Phys. Rev. Lett.* **117**, 093001 (2016).
16. D. Baykusheva, H. J. Wörner, Theory of attosecond delays in molecular photoionization. *J. Chem. Phys.* **146**, 124306 (2017).
17. V. Loriot, A. Marciniak, S. Nandi, G. Karras, M. Hervé, E. Constant, E. Plésiat, A. Palacios, F. Martín, F. Lépine, High harmonic generation-2ω attosecond stereo-photoionization interferometry in N_2. *J. Phys.* **2**, 024003 (2020).
18. S. Nandi, E. Plésiat, S. Zhong, A. Palacios, D. Busto, M. Isinger, L. Neoričić, C. L. Arnold, R. J. Squibb, R. Feifel, P. Decleva, A. L'Huillier, F. Martín, M. Gisselbrecht, Attosecond timing of electron emission from a molecular shape resonance. *Sci. Adv.* **6**, eaba7762 (2020).
19. P. M. Paul, E. S. Toma, P. Breger, G. Mullot, F. Augé, P. Balcou, H. G. Muller, P. Agostini, Observation of a train of attosecond pulses from high harmonic generation. *Science* **292**, 1689–1692 (2001).
20. K. Klünder, J. M. Dahlström, M. Gisselbrecht, T. Fordell, M. Swoboda, D. Guénot, P. Johnsson, J. Caillat, J. Mauritsson, A. Maquet, R. Taïeb, A. L'Huillier, Probing single-photon ionization on the attosecond time scale. *Phys. Rev. Lett.* **106**, 143002 (2011).
21. S. Haessler, B. Fabre, J. Higuet, J. Caillat, T. Ruchon, P. Breger, B. Carré, E. Constant, A. Maquet, E. Mével, P. Salières, R. Taïeb, Y. Mairesse, Phase-resolved attosecond near-threshold photoionization of molecular nitrogen. *Phys. Rev. A* **80**, 011404 (2009).
22. J. Ullrich, R. Moshammer, A. Dorn, R. Dörner, L. P. H. Schmidt, H. Schmidt-Böcking, Recoil-ion and electron momentum spectroscopy: Reaction-microscopes. *Rep. Prog. Phys.* **66**, 1463–1545 (2003).
23. R. Dörner, V. Mergel, O. Jagutzki, L. Spielberger, J. Ullrich, R. Moshammer, H. Schmidt-Böcking, Cold target recoil ion momentum spectroscopy: A 'momentum microscope' to view atomic collision dynamics. *Phys. Rep.* **330**, 95–192 (2000).
24. S. Heuser, A. Jiménez Galán, C. Cirelli, C. Marante, M. Sabbar, R. Boge, M. Lucchini, L. Gallmann, I. Ivanov, A. S. Kheifets, J. M. Dahlström, E. Lindroth, L. Argenti, F. Martín, U. Keller, Angular dependence of photoemission time delay in helium. *Phys. Rev. A* **94**, 063409 (2016).
25. L. Cattaneo, J. Vos, R. Y. Bello, A. Palacios, S. Heuser, L. Pedrelli, M. Lucchini, C. Cirelli, F. Martín, U. Keller, Attosecond coupled electron and nuclear dynamics in dissociative ionization of H_2. *Nat. Phys.* **14**, 733–738 (2018).
26. L. Cattaneo, J. Vos, D. Baykusheva, H. J. Wörner, U. Keller, *Proceedings of ATTO2019* (2019).
27. J. Joseph, F. Holzmeier, D. Bresteau, C. Spezzani, T. Ruchon, J. Hergott, O. Tcherbakoff, P. D'Oliveira, J. Houver, D. Dowek, Angle-resolved studies of XUV–IR two-photon ionization in the RABBITT scheme. *J. Phys. B Atomic Mol. Phys.* **53**, 184007 (2020).
28. J. Vos, L. Cattaneo, S. Patchkovskii, T. Zimmermann, C. Cirelli, M. Lucchini, A. Kheifets, A. S. Landsman, U. Keller, Orientation-dependent stereo Wigner time delay and electron localization in a small molecule. *Science* **360**, 1326–1330 (2018).
29. A. Chacón, M. Lein, C. Ruiz, Asymmetry of Wigner's time delay in a small molecule. *Phys. Rev. A* **89**, 053427 (2014).
30. P. Hockett, E. Frumker, D. M. Villeneuve, P. B. Corkum, Time delay in molecular photoionization. *J. Phys. B Atomic Mol. Phys.* **49**, 095602 (2016).
31. S. Biswas, B. Förg, L. Ortmann, J. Schötz, W. Schweinberger, T. Zimmermann, L. Pi, D. Baykusheva, H. A. Masood, I. Liontos, A. M. Kamal, N. G. Kling, A. F. Alharbi, M. Alharbi, A. M. Azzeer, G. Hartmann, H. J. Wörner, A. S. Landsman, M. F. Kling, Probing molecular environment through photoemission delays. *Nat. Phys.* **16**, 778–783 (2020).
32. Y. Pertot, C. Schmidt, M. Matthews, A. Chauvet, M. Huppert, V. Svoboda, A. Von Conta, A. Tehlar, D. Baykusheva, J. P. Wolf, H. J. Wörner, Time-resolved x-ray absorption spectroscopy with a water window high-harmonic source. *Science* **355**, 264–267 (2017).
33. Y. Hikosaka, E. Shigemasa, Anisotropic fragment emission on valence photoionization of CF_4. *J. Electron Spectrosc. Relat. Phenom.* **152**, 29–32 (2006).
34. K. A. Larsen, C. S. Trevisan, R. R. Lucchese, S. Heck, W. Iskandar, E. Champenois, A. Gatton, R. Moshammer, R. Strom, T. Severt, B. Jochim, D. Reedy, M. Weller, A. L. Landers, J. B. Williams, I. Ben-Itzhak, R. Dörner, D. Slaughter, C. W. McCurdy, T. Weber, T. N. Rescigno, Resonance signatures in the body-frame valence photoionization of CF_4. *Phys. Chem. Chem. Phys.* **20**, 21075–21084 (2018).
35. I. Jordan, H. J. Wörner, Extracting attosecond delays from spectrally overlapping interferograms. *J. Opt.* **20**, 024013 (2018).
36. A. J. Yencha, A. Hopkirk, A. Hiraya, G. Dujardin, A. Kvaran, L. Hellner, M. J. Besnard-Ramage, R. J. Donovan, J. G. Goode, R. R. J. Maier, G. C. King, S. Spyrou, Threshold photoelectron spectroscopy of CF_4 up to 60.5 eV. *J. Electron Spectrosc. Relat. Phenom.* **70**, 29–37 (1994).
37. H. Tachikawa, Ionization dynamics of the small-sized water clusters: A direct ab initio trajectory study. *Chem. Eur. J.* **108**, 7853–7862 (2004).
38. J. Creasey, H. Jones, D. Smith, R. Tuckett, P. Hatherly, K. Codling, I. Powis, Fragmentation of valence electronic states of CF_4^+ and SF_6^+ studied by threshold photoelectron-photoion coincidence spectroscopy. *Chem. Phys.* **174**, 441–452 (1993).

39. B. Brehm, R. Frey, A. Küstler, J. Eland, Kinetic energy release in ion fragmentation: N_2O^+, COS^+ and CF_4^+ decays. *Int. J. Mass Spectrom.* **13**, 251–260 (1974).
40. T. A. Carlson, A. Fahlman, W. Agneta Svensson, M. O. Krause, T. A. Whitley, F. A. Grimm, M. N. Piancastelli, J. W. Taylor, Angle-resolved photoelectron cross section of CF_4. *J. Chem. Phys.* **81**, 3828–3834 (1984).
41. I. Velchev, W. Hogervorst, W. Ubachs, Precision VUV spectroscopy of ArI at 105 nm. *J. Phys. B Atomic Mol. Phys.* **32**, L511–L516 (1999).
42. J. Dahlström, D. Guénot, K. Klünder, M. Gisselbrecht, J. Mauritsson, A. L'Huillier, A. Maquet, R. Taïeb, Theory of attosecond delays in laser-assisted photoionization. *Chem. Phys.* **414**, 53–64 (2013).
43. K. H. Sze, C. E. Brion, Inner-shell and valence-shell electronic excitation of SF_6, SeF_6 and TeF_6 by high energy electron impact: An investigation of potential barrier effects. *Chem. Phys.* **140**, 439–472 (1990).
44. F. Holzmeier, J. Joseph, J.-C. Houver, M. Lebech, D. Dowek, R. R. Lucchese, What causes the angular dependence of photoionization time delays in a shape resonance? arXiv:2107.09915 (2021).
45. C. W. McCurdy, T. N. Rescigno, C. S. Trevisan, R. R. Lucchese, B. Gaire, A. Menssen, M. S. Schöffler, A. Gatton, J. Neff, P. M. Stammer, J. Rist, S. Eckart, B. Berry, T. Severt, J. Sartor, A. Moradmand, T. Jahnke, A. L. Landers, J. B. Williams, I. Ben-Itzhak, R. Dörner, A. Belkacem, T. Weber, Unambiguous observation of F-atom core-hole localization in CF_4 through body-frame photoelectron angular distributions. *Phys. Rev. A* **95**, 011401 (2017).
46. Y.-Y. Yin, C. Chen, D. Elliott, A. Smith, Asymmetric photoelectron angular distributions from interfering photoionization processes. *Phys. Rev. Lett.* **69**, 2353–2356 (1992).
47. M. Sabbar, S. Heuser, R. Boge, M. Lucchini, L. Gallmann, C. Cirelli, U. Keller, Combining attosecond XUV pulses with coincidence spectroscopy. *Rev. Sci. Instrum.* **85**, 103113 (2014).
48. I. Jordan, M. Huppert, D. Rattenbacher, M. Peper, D. Jelovina, C. Perry, A. von Conta, A. Schild, H. J. Wörner, Attosecond spectroscopy of liquid water. *Science* **369**, 974–979 (2020).
49. A. Jain, T. Gaumnitz, A. Bray, A. Kheifets, H. J. Wörner, Photoionization delays in xenon using single-shot referencing in the collinear back-focusing geometry. *Opt. Lett.* **43**, 4510–4513 (2018).
50. A. Jain, T. Gaumnitz, A. Kheifets, H. J. Wörner, Using a passively stable attosecond beamline for relative photoemission time delays at high XUV photon energies. *Opt. Express* **26**, 28604–28620 (2018).
51. J. M. Dahlström, A. L'Huillier, A. Maquet, Introduction to attosecond delays in photoionization. *J. Phys. B Atomic Mol. Phys.* **45**, 183001 (2012).
52. F. A. Gianturco, R. R. Lucchese, N. Sanna, Calculation of low-energy elastic cross sections for electron-CF_4 scattering. *J. Chem. Phys.* **100**, 6464–6471 (1994).
53. A. P. P. Natalense, R. R. Lucchese, Cross section and asymmetry parameter calculation for sulfur 1s photoionization of SF_6. *J. Chem. Phys.* **111**, 5344–5348 (1999).
54. U. Fano, Effects of configuration interaction on intensities and phase shifts. *Phys. Rev.* **124**, 1866–1878 (1961).

Acknowledgments: We thank A. Schneider and M. Seiler for technical support and M. Reiher and C. J. Stein for providing the potential energy surfaces of CF_4^+. **Funding:** We acknowledge funding from the Swiss National Science Foundation (SNSF) through projects 206021_170775 and 200021_172946 and ERC project no. 772797. D.B. acknowledges funding from the SNSF through project P400P2_194343. **Author contributions:** S.H. proposed the study; performed the measurements with contributions of X.G., M.H., J.-B.J., and C.P.; and analyzed the data. X.G. designed and built the experimental setup with contributions from S.H. D.B. developed the theoretical methods and carried out the calculations. H.J.W. supervised the project. S.H., D.B., and H.J.W. wrote the manuscript with input from all coauthors. **Competing interests:** The authors declare that they have no competing interests. **Data and materials availability:** All data needed to evaluate the conclusions in the paper are present in the paper and/or the Supplementary Materials.

Submitted 3 June 2021
Accepted 14 October 2021
Published 3 December 2021
10.1126/sciadv.abj8121